Microstructural, mechanical and shape memory characterizations of Ti−Mo−Sn alloys

Muhammad Luqman HASHMI, Abdul WADOOD

Department of Material Science & Engineering, Institute of Space Technology,
Near Rawat Toll Plaza, Islamabad-44000, Pakistan

Abstract: As a β stabilizing element in Ti-based alloys, the effect of Mo on phase constitution, microstructure, mechanical and shape memory properties was investigated. Different compositions of Ti−xMo−3Sn alloys (where x=2, 4, 6, at.%) were prepared by arc melting. A binary composition of Ti−6Mo alloy was also prepared for comparison. Ti−xMo−3Sn alloys show low hardness and high ductility with 90% reduction in thickness while Ti−6Mo alloy shows high hardness, brittle behavior, and poor ductility. Field emission scanning electron microscopy (FESEM) reveals round morphology of athermal ω (ω_{ath}) precipitates. The presence of ω_{ath} phase is also confirmed by X-ray diffraction (XRD) in both as-cast and solution-treated and quenched conditions. The optical microscopy (OM) and FESEM show that the amount of martensite forming during quenching decreases with an increase in Mo content, which is also due to $\beta \rightarrow \omega$ transformation. The hardness trends reinforce the presence of ω_{ath} too. The shape memory effect (SME) of 9% is the highest for Ti−6Mo−3Sn alloy. The SME is trivial due to ω_{ath} phase formation; however, the increase in SME is observed with an increase in Mo content, which is due to the reverse transformation from ω_{ath} and the stress-induced martensitic transformation. In addition, a new and very simple method was designed and used for shape memory effect measurement.

Key words: Ti−Mo−Sn alloys; shape memory effect; athermal ω phase; martensitic transformation; mechanical properties

1 Introduction

Titanium and titanium alloys have found many applications in marine, automotive, aerospace and biomedical industries [1−4]. Titanium alloys have been investigated as a structural material due to their unique microstructures, mechanical and physical properties [5,6]. There are two allotropes of titanium known as alpha (α) and beta (β). The crystal structure of α is hexagonal closed packed (hcp) while β acquires body-centered cubic (bcc) structure. Pure titanium has $\alpha \rightarrow \beta$ transformation at 1155 K [7]. Aluminum, oxygen, hydrogen, nitrogen, and carbon are added in titanium to stabilize the α phase while vanadium, tantalum, molybdenum, chromium, iron, manganese, nickel and niobium stabilize the β phase even at room temperature. Tin (Sn) is a neutral element and it suppresses the omega (ω) phase precipitation; however, it does not affect the transformation temperatures instead provides solid solution strengthening [8]. The β phase stabilizers when added to titanium matrix, result in the formation of different metastable phases aided by different heat treatments i.e. non-thermo-elastic martensite (α'), thermo-elastic martensite (α'') and hexagonal phases (ω) [9,10].

The commercial-grade pure titanium and other titanium-based alloys are also being widely used in dental implants and orthodontics due to their biocompatibility, bio-functionality, useful mechanical properties and better corrosion

resistance [11]. However, some elements like nickel, aluminum, and vanadium are considered toxic for the human body and studies are being carried out for their replacement [12−14]. The alloys of titanium have been studied in the past decades due to their shape memory properties. Shape memory effect (SME) and superelasticity (SE) are the unique properties due to which these alloys are being used for biomedical applications [15−19]. Titanium−nickel based shape memory alloy was discovered by BUEHLER and coworkers in the Navel-Ordinance-Lab (NOL) [20,21]. Titanium−nickel alloys (commonly known as Nitinol) show excellent shape memory properties; however, it is suspected that Ni present in these alloys is an allergen and toxic to the human body [22,23]. The SME in β titanium alloys was first observed in the Ti−35wt.%Nb alloy system by BAKER in 1971 [24]. Nowadays, nickel-free β titanium shape memory alloys are studied to search for ideal shape memory alloys other than Nitinol [25].

There are two martensitic transformations associated with quenching of β phase in titanium alloys; one is hexagonal closed pack martensite (α') and the other is orthorhombic martensite (α'') [26]. The α' martensite is non-thermo-elastic and the α'' martensite is self-accommodating thermo-elastic, due to which α'' results in the SME because of reversible transformation [27,28]. The α'' martensite and β phases in titanium alloys result in lower elastic modulus under cold worked and solution treated conditions; this property makes these alloys more suitable for biomedical applications [29−33]. The two types of ω phases, isothermal (ω_{iso}, hexagonal) and athermal (ω_{ath}, trigonal), are generally present in the β titanium alloys. The ω_{ath} phase appears during cooling and has a small influence on the deterioration of mechanical properties due to embrittlement while the ω_{iso} phase appears during the aging process and has a greater influence on the deterioration of mechanical properties due to embrittlement of these alloys. The embrittlement of binary titanium alloys during deformation is due to the ω_{iso} phase [34]. However, both of ω phases are produced because of the {111} β-plane collapse along ⟨111⟩ direction [8,35].

In the present study, Mo is added in Ti as a β stabilizing element and Sn is added in a hope that it will improve the workability of Ti−Mo alloys. All elements (Ti, Mo and Sn) used in this research work are biocompatible and bio-functional [36]. The purpose of this research work is to study the effect of increasing Mo content on microstructures and phases of Ti−Mo−3Sn system in as-cast (AC) and solution-treated and quenched (STQ) conditions and to explain the trends of mechanical and shape memory properties based on changes in the microstructures and phases.

2 Experimental

2.1 Materials preparation

Sn-free Ti−6Mo and Sn-added Ti−xMo−3Sn (Ti−2Mo−3Sn, Ti−4Mo−3Sn, and Ti−6Mo−3Sn, at.%) alloy buttons were prepared using arc melting in mini arc melter (MAM 1) in an inert environment using 99.9% pure metals for alloy fabrication. Before melting, metals were ground and cleaned using emery papers and ethanol. 10 g of each alloy system was prepared. The respective mass changes after melting were negligibly small in each alloy system. The prepared buttons were subjected to homogenization in chamber furnace (ENTECH-ECF 8/18) at 1273 K for 2 h in a vacuum environment and then cold-rolled into the plates of about 1 mm in thickness. All alloy systems were encapsulated in quartz tubes, solution treated at 1273 K for 1 h and water quenched by breaking the quartz tubes in water.

2.2 Materials characterization

Field emission scanning electron microscope (FESEM, MIRA3 TESCAN) images and optical micrographs (OM, NOVEX B LED SERIES) were taken for AC and STQ conditions of samples. Similarly, the phases were identified before and after the treatment using X-ray diffraction (XRD, GNR EXPLORER). For SME measurement, the three-point bend test was performed for 5% strain using universal testing machine (UTM, WDW−30) at room temperature and the bending strain (ε_s) was measured for each sample using a digital Vernier caliper. The samples were then heated at 923 K for 1 h followed by air cooling and the residual strain (ε_r) for each sample was measured using Vernier caliper. The hardness of each system was also measured for both AC and STQ conditions by micro Vickers hardness tester (HMV-G). The Ti−6Mo was cracked and shattered into pieces after 1 pass of cold rolling so its characterizations were

performed only for AC compositions.

3 Results and discussion

3.1 Cold workability

The prepared alloy buttons were subjected to cold rolling to measure the workability of the alloys and to form the thin strips for the preparation of the samples for a convenient three-point bend test. The Ti−6Mo sample cracked and shattered into pieces during the first pass of the rolling and showed very poor cold workability. The stereoscopic image of the fractured surface of Ti−6Mo alloy is given in Fig. 1. The workability of the remaining samples is measured as the percentage reduction in thickness where each sample was cold-rolled to a minimum possible thickness by giving 0.2 mm reduction in thickness per pass. Ti−2Mo−3Sn, Ti−4Mo−3Sn, and Ti−6Mo−3Sn were successfully cold-rolled to about 90% reduction in thickness. Sn-free Ti−6Mo shows brittle behavior and poor cold workability; whereas, the addition of Sn plays a role in improving the cold workability of Ti−Mo alloys.
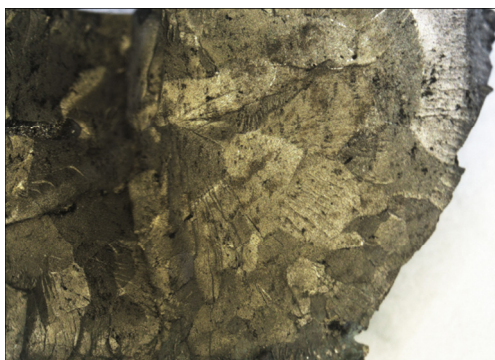

Fig. 1 Stereoscopic image of fractured surface of Ti−6Mo alloy

3.2 Mechanical properties

The hardness of samples in AC and STQ conditions is given in Fig. 2. Among the AC samples, Ti−6Mo has the highest hardness (HV 540). However, with the addition of Sn, the hardness value is reasonably decreased and the minimum hardness (HV 331) is observed for Ti−2Mo−3Sn. This result is in accordance with the cold workability result where Ti−6Mo showed brittle behavior and poor cold workability; whereas, Ti−xMo−3Sn alloys were successfully cold rolled to about 90% cold rolling reduction. For Ti−xMo−3Sn system, 17% increase in the hardness value

(HV 387) is observed for Ti−4Mo−3Sn as compared to Ti−2Mo−3Sn and 8% decrease in hardness (HV 356) is observed for Ti−6Mo−3Sn as compared to Ti−4Mo−3Sn. The similar hardness trend in Ti−xMo−3Sn system is observed for STQ condition but the hardness values of Ti−4Mo−3Sn and Ti−6Mo−3Sn are less as compared to AC condition, which is related to the formation of thermo-elastic martensite (α'') and retained β upon quenching in STQ condition.
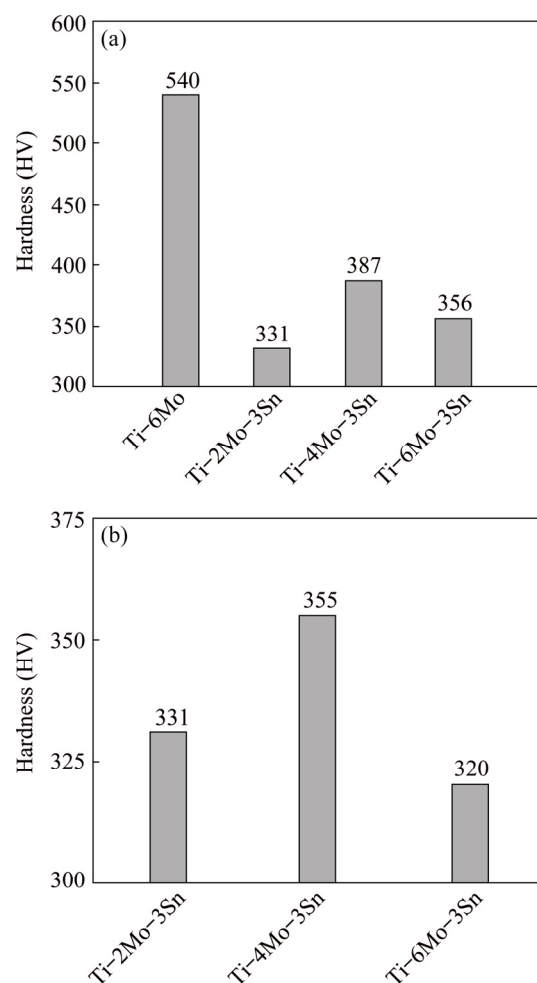

Fig. 2 Hardness of samples in as-cast (AC) condition (a) and solution-treated and quenched (STQ) condition (b)

The effect of different phases for AC and STQ conditions on hardness values is given in Table 1. This hardness trend of both AC and STQ conditions is consistent with the XRD patterns given in Figs. 3, 4 and 5 which confirm the presence of ω_{ath}. The higher hardness of Ti−6Mo alloy is associated with the presence of large amount of α phase as compared to β and ω_{ath}, as shown in XRD pattern given in Fig. 3. For AC condition, we can see that

Table 1 Effect of different phases on hardness values of Ti−xMo−3Sn alloys

AC sample	Phase constitution	Relative change (compared to Ti−2Mo−3Sn)	Hardness (HV)
Ti−2Mo−3Sn	ω_{ath}, α, β	−	331
Ti−4Mo−3Sn	ω_{ath}, α, β	ω_{ath} phase is suppressed, and α and β phases are intensified	387
Ti−6Mo−3Sn	ω_{ath}, α	ω_{ath} phase is intensified, and β phase completely transforms to ω_{ath}	356
STQ sample	Phase Constitution	Relative change (compared to Ti−2Mo−3Sn)	Hardness (HV)
Ti−2Mo−3Sn	ω_{ath}, α'', β	−	331
Ti−4Mo−3Sn	ω_{ath}, α'', β	α'' phase is suppressed	355
Ti−6Mo−3Sn	ω_{ath}, α'', β	ω_{ath} phase is intensified, and α'' and β phases are suppressed	320
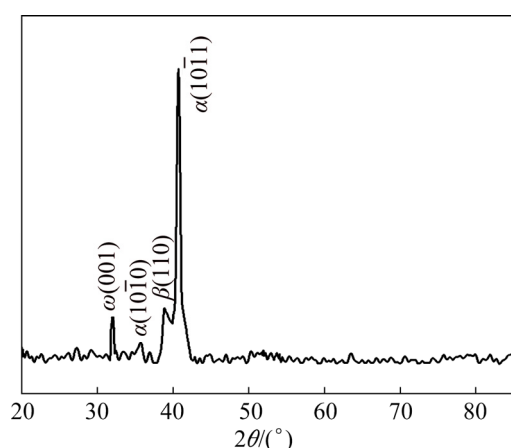
Fig. 3 XRD pattern of Ti−6Mo alloy in as-cast (AC) condition

the ω_{ath} phase is suppressed and the amounts of $\alpha+\beta$ phases are increased for Ti−4Mo−3Sn as compared to Ti−2Mo−3Sn; the highest hardness in Ti−4Mo−3Sn alloy is due to ω_{ath} phase suppression and relatively high amount of α phase. The hardness of Ti−2Mo−3Sn is lower than that of Ti−6Mo−3Sn in AC condition because of the presence of ω_{ath}, α and a relatively small amount of β phase; whereas, the Ti−6Mo−3Sn contains a comparatively large amount of ω_{ath} and α phase but there is no peak of β phase. So, the β as a soft phase and α as strong phase play their roles too in these alloys. However, in STQ samples, the hardness of the Ti−6Mo−3Sn alloy is lower as compared to Ti−2Mo−3Sn; this is because of the complete suppression of α, formation of α'' martensite, retained β and the highest amount of ω_{ath}. Among the samples in STQ condition, the Ti−4Mo−3Sn shows the highest hardness which is similar to the AC condition. It can be seen in XRD profile of samples in STQ condition that intensity
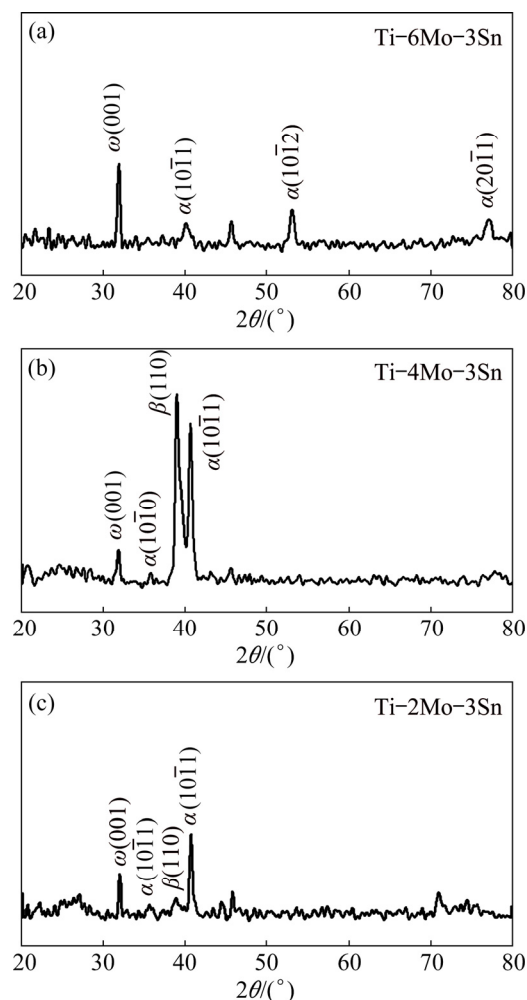
Fig. 4 XRD patterns of Ti−xMo−3Sn alloys in as-cast (AC) condition

of ω_{ath} in Ti−4Mo−3Sn is almost same as for Ti−2Mo−3Sn. But, as we increase the amount of Mo from 2 to 4 at.%, the β phase is not transformed further to ω_{ath} as well as to α'' martensite; so, little higher value of hardness is associated with the
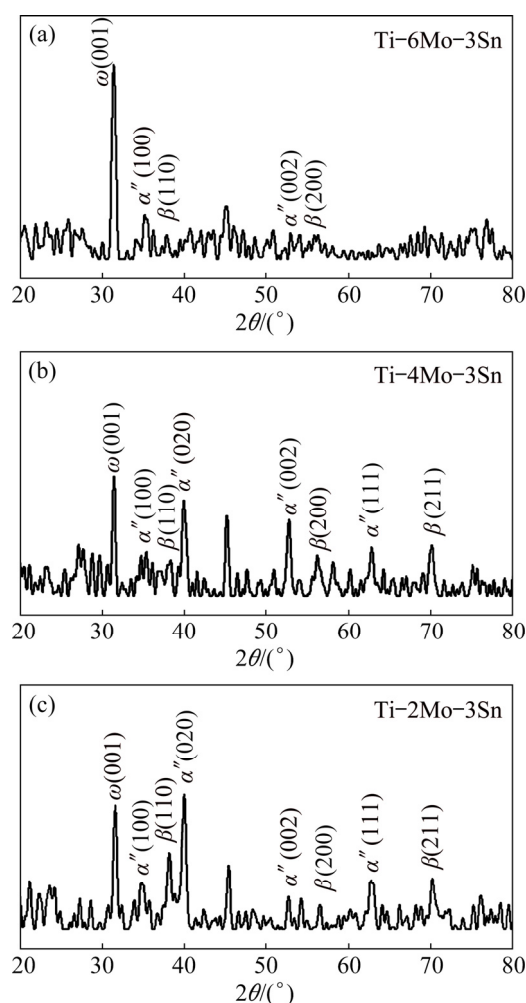
Fig. 5 XRD patterns of Ti−xMo−3Sn alloys in solution-treated and quenched (STQ) condition

effect of relatively strong retained β (among ω_{ath} and α'').

There is a strong role of Sn addition in reducing the hardness as well as avoiding brittle behavior. Sn is also reported as a β stabilizing element [37]. The Ti−6Mo alloy contains large amount of α phase while Ti−xMo−3Sn alloy system has more amount of β as compared to α. However, β-to-ω_{ath} transformation has occurred and ω_{ath} induces ductility in this alloy system. So, we can say that Sn addition can stabilize β phase and thus induces ductility.

The effect of ω_{ath} phase on ductility has also been explained by ZHAO et al [38], and the ductility of Ti−18V and Ti−20V was increased due to the presence of ω_{ath} in solution-treated condition. WADOOD et al [39] have also investigated that ω_{ath} phase assists the martensitic transformation and improves the ductility in titanium-based alloys.

This may be one of the reasons for the lower hardness of alloys having large content of the ω_{ath} phase. The highest ductility in Ti−12Mo alloy is reported in as-quenched condition where $\beta+\omega_{ath}$ structure was formed as compared to heat-treated conditions where the $\beta+\alpha$ structure was observed [40].

3.3 Athermal ω (ω_{ath}) phase

The ω_{ath} phase is easier to form at low cooling rates while the martensitic phase is facilitated by faster cooling rate, i.e. quenching [41,42]. However, the ω_{ath} phase can appear during quenching too [5]. The ω_{iso} phase is believed to appear during low-temperature aging of the β phase [43]. The $\beta\rightarrow\omega$ transformation is different from the martensitic transformation because there are no invariant planes present in ω phase; however, this transformation involves the coordinated motion of atoms. Previous studies on Ti−Nb [42], Ti−Fe [44], Ti−V [45] and Ti−Mo [46] binary alloys have shown that, due to the consideration of elastic-strain-energy, a small lattice-misfit between β and ω results in ellipsoidal morphology while a large misfit causes cuboidal morphologies of these precipitates. The high misfit systems like Ti−V facilitate the formation of cuboidal ω_{iso} phase while the low misfit systems like Ti−Mo facilitate the formation of ellipsoidal ω_{ath} phase [40]. The ellipsoidal morphology of ω_{ath} precipitates is reported in binary Ti−Mo alloy [45]. The ω precipitates in an irregular shape with an average precipitate size around 500 nm, present inside the β (B2) grains, are also reported in Ti−Al−Nb [47] and Ti−Al−Zr [48] systems. The FESEM image of Ti−2Mo−3Sn in AC condition is given in BSE mode in Fig. 6 as a proof of the formation of ω_{ath} phase in Ti−xMo−3Sn system. Precipitates of ω_{ath} phase are less than 500 nm in size and can be seen in almost perfectly round shape distributing uniformly throughout β structure. For further clarification, FESEM images of Ti−6Mo−3Sn are given in SE and BSE modes in Figs. 7(a) and (b). The ω_{ath} precipitates can be seen in both modes; however, BSE mode is used to differentiate different phases based on their contrast that is why the contrast of ω_{ath} is quite clear in BSE mode. This shows that these are not the pits that may have formed during polishing process. If these are surface pits, then these should not appear during BSE mode. The transformation of β to such large
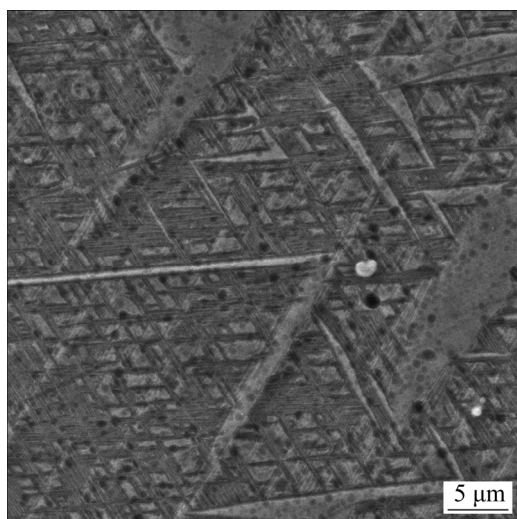
Fig. 6 FESEM image of Ti−2Mo−3Sn alloy in as-cast (AC) condition showing round ω_{ath} precipitates
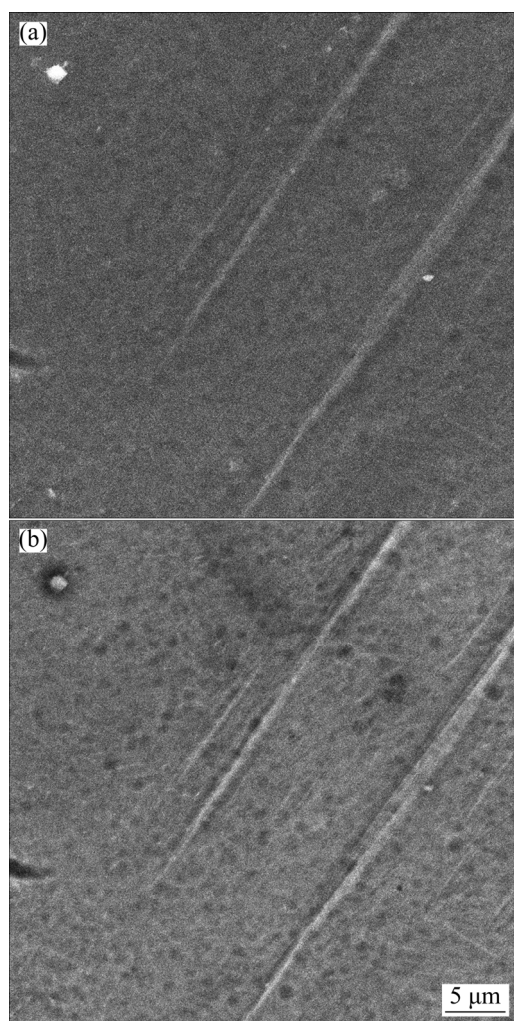

Fig. 7 FESEM images of Ti−6Mo−3Sn alloy in as-cast (AC) condition in SE mode (a) and BSE mode (b) showing precipitates of ω_{ath} (dark spots) due to difference of contrast among phases

extent would have resulted in the homogeneous distribution of ω_{ath}. However, the dots present over the α are needed to be further analyzed and should not be confused with ω_{ath} precipitates or α-to-ω transformation. The round shape of these particles can also be one of the reasons for inducing ductility in Ti−Mo−Sn alloys. However, one thing is quite clear that ω_{ath} phase does play its role in inducing ductility to the Ti−Mo−Sn alloys.

3.4 Phase analysis in as-cast (AC) condition

XRD patterns of AC Ti−6Mo and Ti−xMo−3Sn alloys given in Figs. 3 and 4 respectively confirm the presence of ω_{ath}, α and β phases. The $(10\bar{1}0)$, $(10\bar{1}1)$, $(10\bar{1}2)$ and $(20\bar{1}1)$ basal planes of α appear. The β phase peaks appear on (110) and (200) planes. The (001) plane of ω_{ath} phase appears in all the compositions of AC; it is suppressed for Ti−4Mo−3Sn while turns stronger for Ti−6Mo−3Sn. XRD patterns show that the amount of α phase is higher as compared to the β phase in all AC samples, showing that the α phase has precipitated out during cooling. Optical micrographs and FESEM images of alloys in the AC condition are shown in Figs. 8 and 9, respectively. Optical micrograph of Ti−6Mo given in Fig. 8(a) shows the bright α grain boundaries with grain boundary α plates (α_{GB}), Widmanstätten grain boundary α (α_{WGB}) and Widmanstätten intra-granular α (α_{WI}) at these grain boundaries. Such kind of microstructures with different α phase morphologies were also explained by WADOOD et al [49,50] for Ti−5Cr−3Sn and Ti−6Cr−3Sn alloys. A unique crisscross structure of the α phase and a small amount of dark β are observed within the grains in FESEM image given in Fig. 9(a). The XRD patterns of Ti−6Mo alloy also confirms more amount of α as compared to other phases; low ductility, brittle behavior and very high hardness of Ti−6Mo are related to the presence of this α as a major phase. Optical micrograph of Ti−2Mo−3Sn alloy given in Fig. 8(b) contains α_{GB} within which bright fragmented lamellar α and a small amount of dark β are present. FESEM image given in Fig. 9(b) shows the large amount of fragmented α within the grains. This is consistent with the XRD pattern of this alloy and shows that the α phase is relatively large and the β phase is small. Optical micrograph of Ti−4Mo−3Sn alloy given in Fig. 8(c) shows the dark β grain boundaries and a small amount of
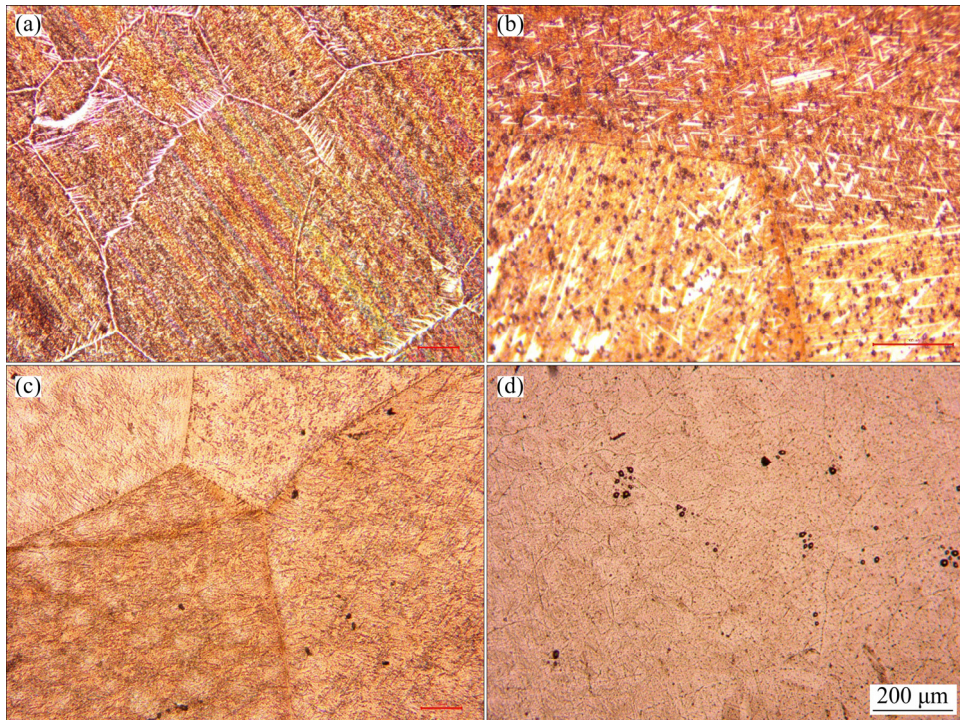
Fig. 8 Optical images of samples in as-cast (AC) condition: (a) Ti−6Mo; (b) Ti−2Mo−3Sn; (c) Ti−4Mo−3Sn; (d) Ti−6Mo−3Sn
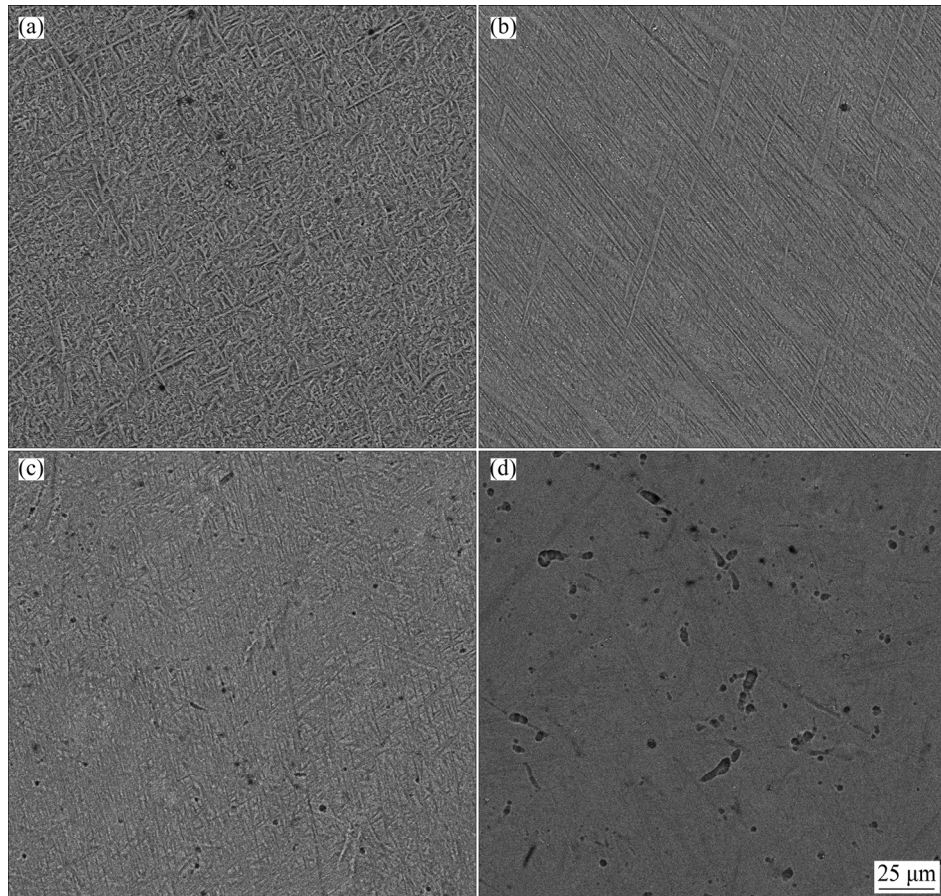

Fig. 9 FESEM images of samples in as-cast (AC) condition: (a) Ti−6Mo; (b) Ti−2Mo−3Sn; (c) Ti−4Mo−3Sn; (d) Ti−6Mo−3Sn

bright α phase within the grains. Its FESEM image given in Fig. 9(c) also shows the fragmented α and dark β within the grains. The XRD pattern of the alloy reveals that the ω phase is suppressed more and is smaller as compared to other compositions; however, the intensity of β as well as α is high, which means that $\beta \rightarrow \omega$ transformation has not taken place in large amount for this alloy system. Optical micrograph of Ti−6Mo−3Sn given in Fig. 8(d) reveals the presence of fragmented lamellar α structure and the β grains and grain boundaries are not observed. Its FESEM image given in Fig. 9(d) shows very light fragment lamellar α contrast and round as well as few coarse ellipsoidal ω_{ath} precipitates. This is an indication of complete $\beta \rightarrow \omega$ transformation but the nano-sized ω precipitates cannot be detected by either optical microscopy or SEM [51]. The XRD pattern of Ti−6Mo−3Sn alloy confirms the highest amount of ω_{ath} phase; moreover, it shows the α phase but there is no β phase peak, which shows that β phase has transformed to ω_{ath} phase. All these microstructures show that the α flakes become thin with increasing Mo content.

3.5 Phase analysis in solution-treated and quenched (STQ) condition

Optical micrographs and FESEM images of samples in STQ condition are given in Figs. 10 and 11, respectively. The effect of quenching on grain size can be seen in these microstructures; the grain size of the STQ samples is much smaller as compared to AC samples. These microstructures of samples in STQ condition show equiaxed β grains and acicular self-accommodating martensite (α'') in Ti−2Mo−3Sn, Ti−4Mo−3Sn and Ti−6Mo−3Sn. However, it can be noticed that the amount of α'' martensite is reduced with increase in the content of Mo and more retained β phase are got in the structure, which shows that the martensitic transformation temperatures are decreased by increasing Mo content. This also shows that Mo acts as a β phase stabilizer in titanium alloys. XRD patterns of STQ samples given in Fig. 5 reinforce the above-mentioned statements. As mentioned earlier, the ω_{ath} (001) peak is also present in STQ samples and it is stronger in Ti−6Mo−3Sn. The α'' has grown on (100), (020), (002) and (111) planes. The β phase grew on (110), (200) and (211) planes. The XRD pattern of Ti−2Mo−3Sn shows that along

with the formation of α'', the ω_{ath} phase still exists and some amount of retained β is also present. The amount of ω_{ath} phase is almost same for Ti−4Mo−3Sn in comparison to Ti−2Mo−3Sn, which means that $\beta \rightarrow \omega$ transformation has not progressed for this composition in STQ condition; moreover, the amount of α'' is decreased and there is more retained β. The XRD pattern of Ti−6Mo−3Sn shows a very small amount of α'' and β but an intensified amount of ω_{ath} phase; the small amount of β and α'' is due to extensive $\beta \rightarrow \omega$ transformation. As mentioned above, the XRD analysis confirms that with the addition of Mo content, the α'' martensite is suppressed; this is due to the reason that the amount $\beta \rightarrow \omega$ transformation is increased by increasing the Mo content.
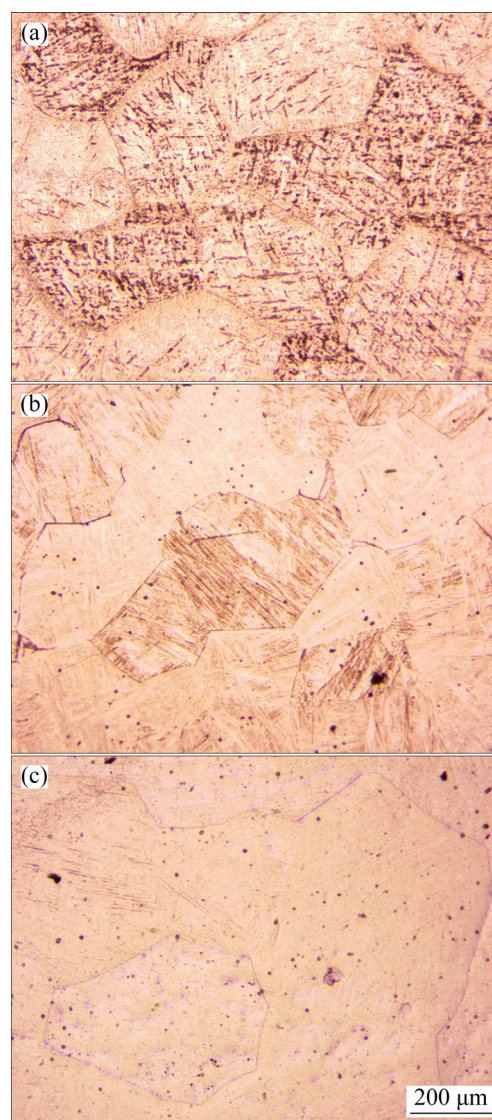

Fig. 10 Optical images of samples in solution-treated and quenched (STQ) condition: (a) Ti−2Mo−3Sn; (b) Ti−4Mo−3Sn; (c) Ti−6Mo−3Sn
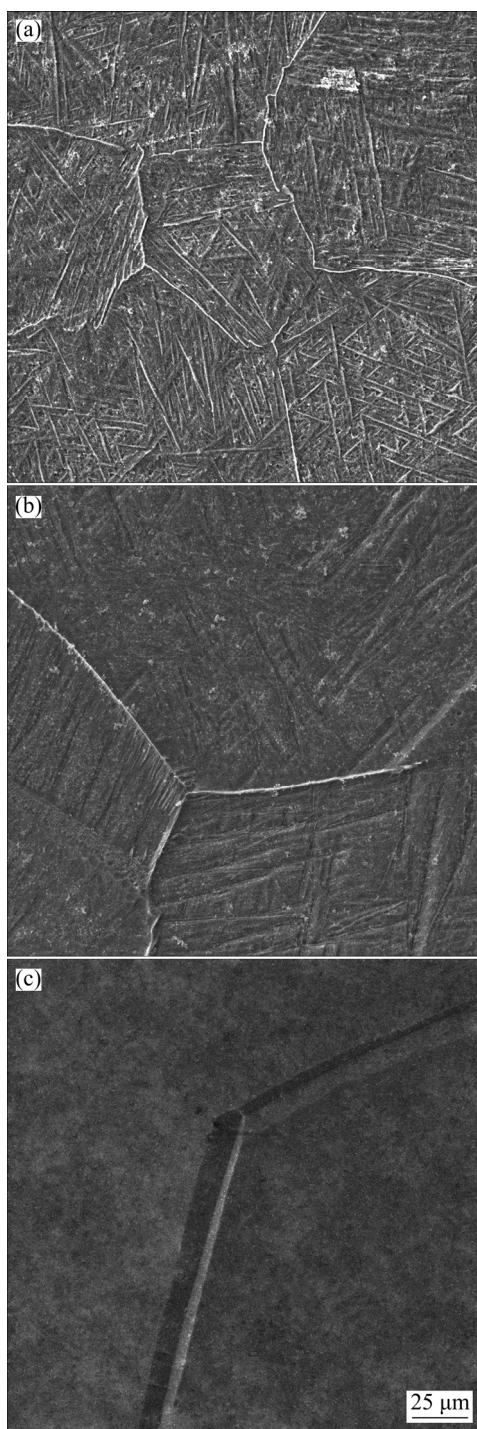
Fig. 11 FESEM images of samples in solution-treated and quenched (STQ) condition: (a) Ti−2Mo−3Sn; (b) Ti−4Mo−3Sn; (c) Ti−6Mo−3Sn

3.6 Shape memory effect

For SME measurement, strips with dimensions of 1 mm × 2 mm × 16 mm were used for a three-point bend test which was performed at 5% applied strain. Different methods for SME measurement are reported [22−25,49,52]. But we

have developed and used a simple method in this research work by using digital Vernier caliper. The schematic given in Fig. 12 explains the process of measurement of shape memory recovery ratios (R_{SME}). As shown in schematic, residual strains after bending (ε_s) and after heating well above the austenite transformation region followed by air cooling (ε_s) were measured. Figure 13 shows the actual values of residual strains and R_{SME} measured by the digital Vernier caliper. The SME was exhibited by Ti−xMo−3Sn alloy system but binary Ti−6Mo alloy showed brittle failure during the cold rolling process. So, we could not use it for SME measurement. This brittle failure is related to α as the dominant phase. The R_{SME} describes the SME and is calculated as follows [39]:

$$R_{SME}=(\varepsilon_s-\varepsilon_r)/\varepsilon_s\times100\% \qquad (1)$$
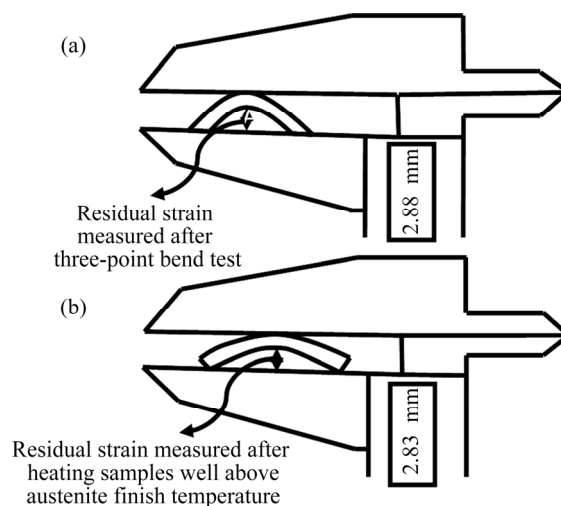

Fig. 12 Schematic showing process of measurement of shape memory recovery ratio using Vernier caliper

In Ti−xMo−3Sn systems, it is observed that the R_{SME} is increased with increasing the content of Mo; that is 3% for Ti−2Mo−3Sn, 5% for Ti−4Mo−3Sn and 9% for Ti−6Mo−3Sn. The increase of R_{SME} is associated with the stress-induced martensitic transformation and austenitic recovery upon heating. The trend of increase in R_{SME} values with respect to an increase in the Mo content is shown in Fig. 14. The shape memory behavior of samples with higher Mo content is associated with the formation of martensite upon bending, which may be facilitated by little bit suppression of ω_{ath} phase during bending. The reverse transformation of ω_{ath} phase under high pressure/load has also been reported previously [53−55]. However, the low values of

After bending   After heating and air cooling

Fig. 13 Measurement of shape memory recovery ratio of Ti−xMo−3Sn alloys using Vernier caliper
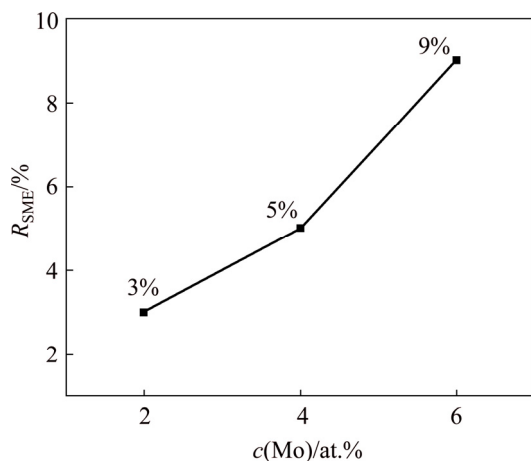

Fig. 14 Shape memory recovery ratio in Ti−xMo−3Sn alloys

R_{SME} are the result of $\beta \rightarrow \omega$ transformation, and by avoiding such transformation completely, the higher R_{SME} values can be achieved.

4 Conclusions

(1) Ti−xMo−3Sn system shows good workability where all compositions can be cold-rolled to about 90% reduction in thickness. Ti−6Mo shows brittle failure during cold rolling due to α as the dominant phase, hence it is not investigated for shape memory properties.

(2) In as-cast Ti−xMo−3Sn alloy system, hardness values are first increased by increasing Mo

content due to a decrease in the β phase and an increase in α phase content. Decrease in the hardness by further increasing Mo content is related to ω_{ath} phase precipitation in a large amount as confirmed by FESEM and XRD. For solution-treated and quenched samples, the hardness trend is almost the same with little lower values of hardness as compared to as-cast samples due to α'' martensite formation.

(3) The quenching process results in the formation of α'' martensite in β grains whose amount decreases with increasing Mo content, which is generally due to an increase in $\beta \rightarrow \omega$ transformation with increasing Mo content.

(4) In Ti−xMo−3Sn system, the shape memory effect is increased by increasing the Mo content. The Ti−6Mo−3Sn shows the highest shape memory effect among all compositions. Relatively higher R_{SME} of Ti−4Mo−3Sn and Ti−6Mo−3Sn is associated with the reverse transformation from ω_{ath} and the formation of stress-induced martensite during the three-point bend test. The calculated shape memory effect is trivial in all compositions, which is due to the transformation of $\beta \rightarrow \omega$. However, the shape memory effect can be increased by avoiding such transformation.

Acknowledgments

References

[1] LEYENS C, PETERS M. Titanium and titanium alloys: Fundamentals and applications [M]. Weinheim: John Wiley & Sons, 2003.

[2] LU J W, ZHAO Y Q, GE P, NIU H Z. Microstructure and beta grain growth behavior of Ti−Mo alloys solution treated [J]. Materials Characterization, 2013, 84: 105−111.

[3] WADOOD A. Brief overview on nitinol as biomaterial [J]. Advances in Materials Science and Engineering, 2016, 2016: 1−9.

[4] JANI J M, LEARY M, SUBIC A, GIBSON M A. A review of shape memory alloy research, applications and opportunities [J]. Materials and Design, 2014, 56: 1078−1113.

[5] BANERJEE D, WILLIAMS J. Perspectives on titanium science and technology [J]. Acta Materialia, 2013, 61: 844−879.

[6] FELLAH M, HEZIL N, LEILA D, SAMAD M A, DJELLABI R, KOSMAN S, MONTAGNE A, IOST A, OBROSOV A, WEISS S. Effect of sintering temperature on structure and tribological properties of nanostructured Ti−15Mo alloy for biomedical applications [J]. Transactions of Nonferrous Metals Society of China, 2019, 29: 2310−2320.

[7] ASKELAND D R, FULAY P P, WRIGHT W J. The science and engineering of materials [M]. 6th ed. Stamford: Cengage Learning, 2010.

[8] RUZIC J, EMURA S, JI X, WATANABE I. Mo segregation and distribution in Ti−Mo alloy investigated using nanoindentation [J]. Materials Science and Engineering A, 2018, 718: 48−55.

[9] KIM H, IKEHARA Y, KIM J, HOSODA H, MIYAZAKI S. Martensitic transformation, shape memory effect and superelasticity of Ti−Nb binary alloys [J]. Acta Materialia, 2006, 54: 2419−2429.

[10] JOSHI V A, Titanium alloys: An atlas of structures and fracture features [M]. Boca Raton: Crc Press, 2006.

[11] KUMAR S, NARAYANAN T S, KUMAR S S. Influence of fluoride ion on the electrochemical behaviour of β-Ti alloy for dental implant application [J]. Corrosion Science, 2010, 52: 1721−1727.

[12] KHAN M, WILLIAMS R L, WILLIAMS D F. The corrosion behaviour of Ti−6Al−4V, Ti−6Al−7Nb and Ti−13Nb−13Zr in protein solutions [J]. Biomaterials, 1999, 20: 631−637.

[13] XIE F, HE X, CAO S, MEI M, QU X. Influence of pore characteristics on microstructure, mechanical properties and corrosion resistance of selective laser sintered porous Ti−Mo alloys for biomedical applications [J]. Electrochimica Acta, 2013, 105: 121−129.

[14] MIYAZAKI S, KIM H Y, HOSODA H. Development and characterization of Ni-free Ti-base shape memory and superelastic alloys [J]. Materials Science and Engineering A, 2006, 438: 18−24.

[15] ELIAS C, LIMA J, VALIEV R, MEYERS M. Biomedical applications of titanium and its alloys [J]. JOM: The Journal of the Minerals, Metals & Materials Society, 2008, 60: 46−49.

[16] BALAZIC M, KOPAC J, JACKSON M J, AHMED W. Titanium and titanium alloy applications in medicine [J]. International Journal of Nano and Biomaterials, 2007, 1: 3−34.

[17] NIINOMI M. Mechanical biocompatibilities of titanium alloys for biomedical applications [J]. Journal of the Mechanical Behavior of Biomedical Materials, 2008, 1: 30−42.

[18] MACHADO L, SAVI M. Medical applications of shape memory alloys [J]. Brazilian Journal of Medical and Biological Research, 2003, 36: 683−691.

[19] KIM J I, KIM H Y, HOSODA H, MIYAZAKI S. Shape memory behavior of Ti−22Nb−(0.5−2.0)O (at%) biomedical alloys [J]. Materials Transactions, 2005, 46: 852−857.

[20] KAUFFMAN G B, MAYO I. The story of nitinol: The serendipitous discovery of the memory metal and its applications [J]. The Chemical Educator, 1997, 2: 1−21.

[21] GALLARDO-FUENTES J M, GÜMPEL P, STRITTMATTER J. Phase change behavior of nitinol shape memory alloys [J]. Advanced Engineering Materials, 2002, 4: 437−452.

[22] EL-FENINAT F, LAROCHE G, FISET M, MANTOVANI D. Shape memory materials for biomedical applications [J]. Advanced Engineering Materials, 2002, 4: 91−104.

[23] BAHADOR A, HAMZAH E, KONDOH K, ABUBAKAR T A, YUSOF F, UMEDA J, IBRAHIM M K. Microstructure and superelastic properties of free forged Ti−Ni shape-memory alloy [J]. Transactions of Nonferrous Metals Society of China, 2018, 28: 502−514.

[24] BAKER C. The shape-memory effect in a titanium−35 wt.% niobium alloy [J]. Metal Science Journal, 1971, 5: 92−100.

[25] BIESIEKIERSKI A, WANG J, GEPREEL M A, WEN C. A new look at biomedical Ti-based shape memory alloys [J]. Acta Biomaterialia, 2012, 8: 1661−1669.

[26] MAESHIMA T, USHIMARU S, YAMAUCHI K, NISHIDA M. Effect of heat treatment on shape memory effect and superelasticity in Ti−Mo−Sn alloys [J]. Materials Science and Engineering A, 2006, 438: 844−847.

[27] VAN-HUMBEECK J. Damping capacity of thermoelastic martensite in shape memory alloys [J]. Journal of Alloys and Compounds, 2003, 355: 58−64.

[28] SHARIFI E M, KERMANPUR A. Superelastic properties of nanocrystalline NiTi shape memory alloy produced by thermomechanical processing [J]. Transactions of Nonferrous Metals Society of China, 2018, 28: 515−523.

[29] ZHOU Y L, NIINOMI M, AKAHORI T. Effects of Ta content on Young's modulus and tensile properties of binary Ti−Ta alloys for biomedical applications [J]. Materials Science and Engineering A, 2004, 371: 283−290.

[30] COLLINGS E. The physical metallurgy of titanium alloys [M]. 3rd ed. Ohio: Metals Park Ohio, 1984.

[31] ROBARE E, BUGLE C, DAVIDSON J. Development of processing methods for Ti−13Nb−13Zr [J]. Advances in the Science and Technology of Titanium Alloy Processing, 1996, 1996: 283−291.

[32] MATSUMOTO H, WATANABE S, HANADA S. Beta TiNbSn alloys with low Young's modulus and high strength [J]. Materials Transactions, 2005, 46: 1070−1078.

[33] ZHOU Y L, LUO D M. Microstructures and mechanical properties of Ti−Mo alloys cold-rolled and heat treated [J]. Materials Characterization, 2011, 62: 931−937.

[34] MAESHIMA T, NISHIDA M. Shape memory properties of biomedical Ti−Mo−Ag and Ti−Mo−Sn alloys [J]. Materials Transactions, 2004, 45: 1096−1100.

[35] DEVARAJ A, NAG S, SRINIVASAN R, WILLIAMS R, BANERJEE S, BANERJEE R, FRASER, H L. Experimental evidence of concurrent compositional and structural instabilities leading to ω precipitation in titanium–molybdenum alloys [J]. Acta Materialia, 2012, 60: 596−609.

[36] KURODA D, NIINOMI M, MORINAGA M, KATO Y, YASHIRO T. Design and mechanical properties of new β type titanium alloys for implant materials [J]. Materials Science and Engineering A, 1998, 243: 244−249.

[37] ZHANG D, YANG S, WEI M, MAO Y, TAN C, LIN J. Effect of Sn addition on the microstructure and superelasticity in Ti−Nb−Mo−Sn alloys [J]. Journal of the Mechanical Behavior of Biomedical Materials, 2012, 13: 156−165.

[38] ZHAO X, NIINOMI M, NAKAI M, HIEDA J. Effect of deformation-induced ω phase on the mechanical properties of metastable β-type Ti−V alloys [J]. Materials Transactions, 2012, 53: 1379−1384.

[39] WADOOD A, INAMURA T, HOSODA H, MIYAZAKI S. Ageing behavior of Ti−6Cr−3Sn β titanium alloy [J]. Materials Science and Engineering A, 2011, 530: 504−510.

[40] SUN F, PRIMA F, GLORIANT T. High-strength nanostructured Ti−12Mo alloy from ductile metastable beta state precursor [J]. Materials Science and Engineering A, 2010, 527: 4262−4269.

[41] TOMIO Y, FURUHARA T, MAKI T. Effect of cooling rate on superelasticity and microstructure evolution in Ti−10V−2Fe−3Al and Ti−10V−2Fe−3Al−0.2 N alloys [J]. Materials Transactions, 2009, 2009: 909280900.

[42] MOFFAT D, LARBALESTIER D. The compctition between martensite and omega in quenched Ti−Nb alloys [J]. Metallurgical Transactions A, 1988, 19: 1677−1686.

[43] PANG E, PICKERING E, BAIK S I, SEIDMAN D N, JONES N G. The effect of zirconium on the omega phase in Ti−24Nb−[0−8]Zr (at.%) alloys [J]. Acta Materialia, 2018, 153: 62−70.

[44] WILLIAMS J, BLACKBURN M. The influence of misfit on the morphology and stability of the omega phase in titanium transition metal alloys [R]. North American Rockwell Science Center, 1969.

[45] MENON E S, KRISHNAN R. Phase transformations in Ti−V alloys [J]. Journal of Materials Science, 1983, 18: 365−374.

[46] DEVARAJ A, WILLIAMS R, NAG S, SRINIVASAN R, FRASER H, BANERJEE R. Three-dimensional morphology and composition of omega precipitates in a binary titanium–molybdenum alloy [J]. Scripta Materialia, 2009, 61: 701−704.

[47] SONG L, ZHANG L, XU X, SUN J, LIN J. Omega phase in as-cast high-Nb-containing TiAl alloy [J]. Scripta materialia, 2013, 68: 929−932.

[48] JIANG H, HU D, WU X. Thermal stability of the omega phase in Zr-containing TiAl alloys [J]. Journal of Alloys and Compounds, 2009, 475: 134−138.

[49] WADOOD A, INAMURA T, HOSODA H, MIYAZAKI S. Comparative study of Ti−xCr−3Sn alloys for biomedical applications [J]. Materials Transactions, 2011, 52: 1787−1793.

[50] WADOOD A, INAMURA T, HOSODA H, MIYAZAKI S. Effect of α phase precipitation on martensitic transformation and mechanical properties of metastable β Ti−6Cr−3Sn

biomedical alloy [J]. Journal of Alloys and Compounds, 2013, 577: s427−s430.

[51] ZHÁNAL P, HARCUBA P, HÁJEK M. Microstructural changes in β-Ti alloy investigated by electrical resistance [C]//WDS'15 Proceedings of Contributed Papers−Physics. 2015: 54−60.

[52] KHAN A N, MUHYUDDIN M, WADOOD A. Development and characterization of nickel–titanium–zirconium shape memory alloy for engineering applications [J]. Russian Journal of Non-Ferrous Metals, 2017, 58: 509−515.

[53] TALLING R, DASHWOOD R, JACKSON M, DYE D. On the mechanism of superelasticity in Gum metal [J]. Acta Materialia, 2009, 57: 1188−1198.

[54] YANG Y, LI G P, CHENG G M, LI Y L, YANG K. Multiple deformation mechanisms of Ti−22.4Nb−0.73Ta−2.0Zr−1.34O alloy [J]. Applied Physics Letters, 2009, 94: 061901.

[55] DEY G K, TEWARI R, BANERJEE S, JYOTI G, GUPTA S C, JOSHI K D, SIKKA S K. Formation of a shock deformation induced ω phase in Zr 20 Nb alloy [J] Acta Materialia, 2004, 52: 5243−5254.

Ti−Mo−Sn 合金显微组织、力学性能和形状记忆性能

Muhammad Luqman HASHMI, Abdul WADOOD

Department of Material Science & Engineering, Institute of Space Technology,

Near Rawat Toll Plaza, Islamabad-44000, Pakistan

摘　要：研究 Mo 作为 β 相稳定元素，对 Ti−Mo−Sn 合金相组成、显微组织、力学性能和形状记忆性能的影响。通过电弧熔炼法制备不同成分的 Ti−xMo−3Sn (x=2，4，6，摩尔分数，%)合金，并制备二元合金 Ti−6Mo 作为对照组。Ti−xMo−3Sn 合金具有硬度低和韧性高(厚度可减少 90%)的特点，而 Ti−6Mo 合金则表现出脆性行为，硬度高、韧性差。场发射扫描电镜(FESEM)下发现圆形的无热 ω (ω_{ath})析出相。X 射线衍射结果也证实铸态和固溶处理−淬火态的样品中均存在 ω_{ath} 相。光学显微镜和 FESEM 结果显示，由于发生 β→ω 相变，淬火过程中形成的马氏体数量随着 Mo 含量的增加而降低。硬度的变化趋势也证实 ω_{ath} 相的存。Ti−6Mo−3Sn 合金的形状记忆效应(SME) 最高，为 9%。合金 SME 较低是由于形成 ω_{ath} 相；然而，SME 随着 Mo 含量的增加而增加，这是由于 ω_{ath} 相的逆相变和由压力引起的马氏体相变所致。另外，设计一种新的、非常简单的测量形状记忆效应的方法。

关键词：Ti−Mo−Sn 合金；形状记忆效应；无热 ω 相；马氏体相变；力学性能

(Edited by Bing YANG)